Spatio-Temporal Analysis and Modeling of Distributed Photovoltaic Contributions to Distribution Network Safety

Huan YAN[1], Yuanyuan YUE[1], Honggang JIA[1], Zijia HUI[1], and Hao ZENG[2,*]

[1] State Grid Shaanxi Electric Power Company Limited Research Institute, Xi'an, China
[2] Chongqing Electric Energy Star Co., Ltd, Chongqing, China
[*] Corresponding author. E-mail: zenghao0409@163.com

Received: April 26, 2026; Accepted: July. 30, 2026

The large-scale integration of distributed photovoltaic (DPV) systems introduces significant spatio-temporal variability into distribution networks, posing challenges to voltage stability, line loading, and protection coordination. This paper proposes a spatio-temporal analysis and modeling framework to quantify the safety impacts of DPV contributions. By integrating spatial topology characteristics with temporal generation-load fluctuations, the proposed model evaluates dynamic safety margins under varying penetration scenarios. A composite load model incorporating ZIP components, induction motor dynamics, and a simplified PV subsystem is established, and a reinforcement learning-enhanced Grey Wolf Optimizer (RL-GWO) is developed for high-precision parameter identification. Case studies demonstrate its effectiveness in identifying high-risk nodes and revealing critical spatio-temporal coupling effects, providing analytical support for distribution network planning and secure operation, while showing that appropriate DPV penetration can significantly improve voltage profiles and reduce network losses.

Keywords: Distributed photovoltaic; Spatio-temporal Analysis; Parameter Identification; Reinforcement learning; Distribution Network Security; Grey Wolf Optimizer

http://dx.doi.org/10.6180/jase.202611_34.045

1. Introduction

The global transition toward low-carbon energy systems has catalyzed unprecedented growth in distributed photovoltaic (DPV) deployment, driven by declining installation costs, supportive policy frameworks, and the imperative to achieve carbon neutrality targets. In China, the "dual carbon" goals have further accelerated DPV penetration across both urban and rural distribution networks, fundamentally transforming the traditional paradigm of passive, unidirectional power delivery into an active, bidirectional system with highly stochastic generation profiles [1]. While DPV integration confers compelling environmental and economic benefits—including reduced carbon emissions, alleviated transmission congestion, and enhanced local energy self-sufficiency—its large-scale adoption introduces pronounced spatiotemporal variability that poses formidable challenges to voltage stability, line loading, and protection coordination. Unlike conventional generation, DPV output is governed by meteorological conditions, creating dynamic generation–load mismatches whose severity and spatial distribution vary continuously throughout the day and across seasons. Systematically characterizing and quantifying these spatiotemporal security impacts is therefore essential for the safe planning and operation of high-penetration distribution networks.

To provide a systematic and clearly structured account of the state of the art, the existing literature on the security implications of DPV integration is reorganized here into three core research branches, namely (i) voltage/power-quality control, (ii) DPV hosting-capacity evaluation, and

(iii) optimization and control algorithms for planning and operation, followed by an explicit summary of the unified research gap that these three branches collectively leave open.

The adverse effects of DPV integration on power quality and voltage security have received sustained research attention. High DPV penetration is particularly associated with nodal voltage overruns at grid connection points, where reverse power injection during peak irradiance periods can drive voltages beyond permissible limits. To predict and preempt such violations, data-driven approaches have been extensively explored. Hybrid deep learning models combining Transformer architectures with bidirectional long short-term memory (BiLSTM) networks have demonstrated superior accuracy in anticipating voltage overruns [2], while eXtreme gradient boosting coupled with time convolutional networks (XGBoost-TCN) has been applied to high-precision voltage prediction in DPV-rich feeders [3]. These methods offer valuable operational decision support; however, they are inherently data-driven and retrospective in nature—their predictive performance is contingent on historical data that may inadequately represent novel or extreme penetration scenarios not yet observed in the operational record. Voltage coordination at the network level has been addressed through distributed model predictive control (DMPC), which decomposes the control problem into regional subproblems to reduce computational burden and communication overhead [4]. Although DMPC achieves improved voltage compliance, its effectiveness depends critically on accurate local state estimation and inter-region information exchange—conditions that may be difficult to sustain in rural feeders with sparse telemetry infrastructure. Harmonic pollution introduced by DPV inverters constitutes a parallel power quality threat; improved particle swarm optimization (PSO)-based harmonic suppression strategies have been shown to reduce grid-connected current distortion [5], and maximum likelihood estimation (MLE) of harmonic parameters has been employed to characterize harmonic injection and evaluate hosting capacity under harmonic constraints [6]. In addition, protection coordination is also affected by DPV-induced power-quality disturbances: multi-terminal negative sequence directional pilot protection methods have been developed to address altered fault current signatures introduced by DPV [19], and lightning risk assessment of active distribution networks with DPV has revealed that the interaction between photovoltaic installations and adjacent distribution line towers can significantly increase the lightning trip rate of nearby towers [20]. While these contributions represent meaningful advances, they collectively address voltage, harmonic, and protection-related phenomena in isolation rather than as components of an integrated security margin framework that also captures voltage and thermal loading dynamics in a spatiotemporally resolved manner.

Assessment of DPV hosting and carrying capacity—the maximum DPV penetration a network can accommodate without violating operational constraints—forms a second major research strand. Reinforcement learning (RL) has emerged as a promising tool for navigating the high-dimensional, nonlinear feasibility space of this problem; a Deep Deterministic Policy Gradient (DDPG)-based approach has been proposed to evaluate carrying capacity in IEEE-33 bus systems [7], demonstrating the ability to handle complex nonlinear constraints. Nevertheless, DDPG-based frameworks require extensive offline training and may exhibit degraded transferability when feeder topology or penetration patterns deviate materially from training conditions. Improved simulated annealing has been applied to adaptive modeling of distributed PV absorptive capacity [8]; this approach yields promising results but relies on a simplified model that may not fully reproduce the dynamic interactions between composite loads and inverter-interfaced generation under disturbance conditions. Economic access capacity evaluation methods incorporating active and reactive power regulation, combined with K-means clustering-based scenario generation and second-order cone relaxation, have been proposed for assessing maximum DPV integration capacity [9]. Robust assessment methods for mountainous distribution networks have introduced soft open points (SOPs) and energy storage to improve flexibility and hosting capacity [10]. A distributionally robust optimization framework based on Kullback-Leibler (KL) divergence has been applied to photovoltaic-storage expansion planning [11]; however, the focus on planning-stage decisions means that real-time spatiotemporal security dynamics during operation remain insufficiently characterized.

Optimization and control methods represent a third major category of responses to DPV integration challenges. Active power scheduling frameworks for large-scale urban distribution networks have incorporated the regulation capacity of the main network gas units to minimize PV curtailment [12]. Day-ahead dispatch strategies leveraging LSTM-Transformer-based photovoltaic forecasting in conjunction with distributed pumped-storage hydropower have demonstrated improved renewable integration [13]. Multi-objective optimization algorithms—including the multi-objective coati optimization algorithm (MOCOA) [14], the improved beluga whale optimization (IBWO) algorithm [15], and distributed voltage optimal control for energy storage systems [1]—have achieved notable reductions in network losses and voltage deviations. Quantum genetic algorithm (QGA)-based line loss optimization provides valuable analytical insights for low-voltage networks with DPV [2], and optical-storage direct-flexible consumption modes address DPV digestion efficiency [16]. Energy storage siting and sizing under multiple scenarios based on improved affinity propagation clustering has been proposed to alleviate voltage violations and reduce network losses arising from mismatched DPV deployment [17]. Enhanced LSTM-based load forecasting methods for low-voltage DPV distribution networks improve dispatch accuracy [18], but high forecasting precision alone cannot quantify the underlying network security boundaries under varying penetration levels.

A critical gap that traverses the aforementioned literature is the absence of a unified framework that simultaneously resolves the spatial topology of the distribution feeder and the temporal dynamics of the generation–load interaction to produce spatiotemporally resolved, node-level security margins under multiple DPV penetration scenarios. To fill these gaps, this paper presents an integrated spatiotemporal analysis and modeling framework that quantifies the security impact of DPV penetration on active distribution systems. The proposed framework couples spatial feeder topology with temporal generation–load fluctuation data to evaluate dynamic security margins across multiple penetration scenarios. A composite load model is established and coupled with a reinforcement learning-enhanced Grey Wolf Optimizer (RL-GWO), in which Q-learning adaptively schedules five search operators to overcome premature convergence and local-optima entrapment inherent in conventional metaheuristics. Case studies are conducted on a real 10 kV feeder to validate the proposed approach. The main contributions of this paper are as follows:

(1) An integrated spatiotemporal analysis framework is proposed that jointly resolves the spatial distribution of DPV installations across feeder nodes and the temporal dynamics of generation–load interaction, producing quantitative, node-level security margin maps across multiple penetration scenarios.

(2) A composite load model comprising ZIP static components, induction motor dynamics, and a PV source subsystem is established to accurately simulate mixed-load distribution feeders, addressing the systematic underestimation of voltage sensitivity inherent in conventional static load representations.

(3) An RL-GWO algorithm is developed for high-precision composite load parameter identification, in which Q-learning adaptively schedules five search operators to balance exploration and exploitation, overcoming the premature convergence and local-optima entrapment that afflict conventional metaheuristic optimizers applied to high-dimensional parameter spaces.

(4) The proposed framework is validated on a real 10 kV feeder, providing quantitative insights into voltage and network-loss variations under different DPV penetration levels, thereby offering actionable analytical support for distribution network planning and safe operation under high DPV penetration.

2. Materials and methods

2.1. Composite Load Model with Distributed PV

To model the aggregate behavior of a distribution node hosting DPV generation, a composite source–load equivalent is adopted. The node is treated as a compact entity that preserves the original network power response. The power balance equations are:

$$\begin{cases} P = P_{\mathrm{D}} + P_{\mathrm{zip}} + P_{\mathrm{M}} - P_{\mathrm{pv}} \\ Q = Q_{\mathrm{D}} + Q_{\mathrm{zip}} + Q_{\mathrm{M}} - Q_{\mathrm{pv}} \end{cases} \tag{1}$$

where P and Q are the net active and reactive power injections at the composite node; P_{D} and Q_{D} denote the active and reactive power consumed by the equivalent distribution-network impedance; P_{M} and Q_{M} are the active and reactive power of the induction motor component; P_{zip} and Q_{zip} represent the ZIP static load; and P_{pv}, Q_{pv} are the active and reactive output power of the PV system. Equation (1) is purely algebraic and, by itself, characterizes only the steady-state power balance at the composite node. The induction motor term $(P_{\mathrm{M}}, Q_{\mathrm{M}})$ is in fact the output of a set of nonlinear differential equations describing the motor's electromechanical transient behavior; these dynamic equations are developed, together with Eq. (1), elevate the composite load model from a static equivalent to a differential–algebraic (DAE) system suitable for transient security analysis.

2.2. ZIP Static Load Model

The static load fraction is modelled by the standard ZIP polynomial, which captures voltage-dependent constant-impedance (Z), constant-current (I), and constant-power (P) characteristics, extended with frequency-sensitivity terms:

$$\begin{cases} P_{\mathrm{zip}} = P_{\mathrm{L0}}\left[Z_{\mathrm{p}}\left(\frac{U_{\mathrm{L}}}{U_{\mathrm{L0}}}\right)^2 + I_{\mathrm{p}}\frac{U_{\mathrm{L}}}{U_{\mathrm{L0}}} + P_{\mathrm{p}}\right](1 + L_{\mathrm{P}}\,\Delta f) \\ Q_{\mathrm{zip}} = Q_{\mathrm{L0}}\left[Z_{\mathrm{q}}\left(\frac{U_{\mathrm{L}}}{U_{\mathrm{L0}}}\right)^2 + I_{\mathrm{q}}\frac{U_{\mathrm{L}}}{U_{\mathrm{L0}}} + P_{\mathrm{q}}\right](1 + L_{\mathrm{Q}}\,\Delta f) \end{cases} \tag{2}$$

where P_{L0} and Q_{L0} are the rated active and reactive load power at the reference terminal voltage U_{L0}; L_{P} and L_{Q} are the active and reactive frequency-sensitivity coefficients after PV grid connection; Z_{p}, I_{p}, P_{p} and Z_{q}, I_{q}, P_{q} are the constant-impedance, constant-current, and constant-power coefficients for active and reactive power, respectively.

2.3. Induction Motor Transient Model

Unlike the ZIP load, whose response to a voltage disturbance is instantaneous and purely algebraic, the induction motor component—which typically accounts for a substantial share of the active demand on distribution feeders—possesses electromechanical inertia and must therefore be described by differential equations if the composite load model is to reproduce transient security phenomena rather than only steady-state operating points. The motor is represented by the standard third-order electromechanical transient model:

$$\dot{U}_{\mathrm{L}} = \dot{E}' + (R_{\mathrm{s}} + jX')\,\dot{I}_{\mathrm{M}} \tag{3}$$

$$\frac{d\dot{E}'}{dt} = -js\dot{E}' - \frac{\dot{E}' - j(X - X')\dot{I}_{\mathrm{M}}}{T_{d0}} \tag{4}$$

$$\frac{ds}{dt} = \frac{1}{T_{\mathrm{j}}}(T_{\mathrm{M}} - T_{\mathrm{E}}) \tag{5}$$

$$I_{\mathrm{Md}} = \frac{R_{\mathrm{s}}(U_d - E'_d) + X'(U_q - E'_q)}{R_{\mathrm{s}}^2 + X'^2} \tag{6}$$

$$I_{\mathrm{Mq}} = \frac{R_{\mathrm{s}}(U_q - E'_q) - X'(U_d - E'_d)}{R_{\mathrm{s}}^2 + X'^2} \tag{7}$$

$$\begin{aligned} &X' = X_{\mathrm{s}} + \frac{X_{\mathrm{m}}X_{\mathrm{r}}}{X_{\mathrm{m}} + X_{\mathrm{r}}}, \qquad T_{\mathrm{E}} = E'_d I_{\mathrm{Md}} + E'_q I_{\mathrm{Mq}}, \\ &T_{\mathrm{M}} = \left(A\omega_{\mathrm{r}}^2 + B\omega_{\mathrm{r}} + C\right)T_0, \qquad \omega_{\mathrm{r}} = 1 - s \end{aligned} \tag{8}$$

where $\dot{E}' = E'_d + jE'_q$ is the transient EMF behind the transient reactance X'; s is the rotor slip; $\dot{I}_{\mathrm{M}} = I_{\mathrm{Md}} + jI_{\mathrm{Mq}}$ is the motor stator current; R_{s}, X, X_{s}, X_{r}, X_{m} are the stator resistance, rotor locked-rotor reactance, stator leakage reactance, rotor leakage reactance, and magnetizing reactance, respectively; T_{d0} is the rotor open-circuit time constant; T_{j} is the equivalent inertia time constant; T_{E} and T_{M} are the electromagnetic and mechanical torques; T_0 is the initial (pre-disturbance) mechanical torque; and A, B, C (with $A + B + C = 1$) are load-torque coefficients characterizing the torque–speed dependence of the driven mechanical load. The motor's contribution to the composite node power balance of Eq. (1) is then

$$P_{\mathrm{M}} = U_d I_{\mathrm{Md}} + U_q I_{\mathrm{Mq}}, \qquad Q_{\mathrm{M}} = U_q I_{\mathrm{Md}} - U_d I_{\mathrm{Mq}} \tag{9}$$

Equations (3)–(9) form a set of nonlinear ordinary differential equations in the state variables $(\dot{E}', s)$, driven by the instantaneous node voltage $\dot{U}_{\mathrm{L}}$, and are integrated jointly with the algebraic ZIP equations (2) and the PV output equations of Section 2.5 at every simulation time step, as detailed in Section 2.4.

2.4. Interaction of the ZIP, Motor, and PV Subsystems under Disturbance

The three subsystems of the composite node are coupled solely through the shared terminal voltage $\dot{U}_{\mathrm{L}}$ and the instantaneous power balance of Eq. (1), yet they respond to a common disturbance—such as a voltage sag triggered by a nearby feeder fault or by abrupt DPV output curtailment—on markedly different time scales, giving rise to a characteristic three-stage interaction pattern.

(i) Because the ZIP load of Eq. (2) is purely algebraic in U_{L}, its power consumption tracks the voltage sag instantaneously: the constant-impedance term reduces power quadratically with U_{L}, the constant-current term reduces power linearly, and the constant-power term attempts to hold power constant by increasing its current draw as U_{L} falls, the latter effect acting as a secondary contributor to voltage depression.

(ii)The motor cannot adjust its electromagnetic torque T_{E} instantaneously, since the transient EMF $\dot{E}'$ evolves according to the first-order lag of Eq. (4) with time constant T_{d0}. During the sag, T_{E} (which scales approximately with U_{L}^2) falls below the mechanical load torque T_{M}, so the slip s increases per Eq. (5) (the motor decelerates); the growing slip increases the reactive current I_{Mq} drawn from the network via Eq. (7), which further depresses U_{L} at the composite node—a self-reinforcing mechanism consistent with the fault-induced delayed voltage recovery (FIDVR) phenomenon reported for motor-dominated feeders. After fault clearance, the slip decays back toward its pre-disturbance value on a time scale governed jointly by T_{d0} and T_{j}, so the motor's reactive-power influence on U_{L} persists for hundreds of milliseconds after the ZIP load has already returned to its pre-disturbance operating point.

(iii) The PV subsystem responds fastest of the three, since its output is governed by the power-electronic

MPPT/inverter control loop of Section 2.6 rather than by electromechanical inertia. Under the sag, the array operating point shifts along the I–U characteristic of Eq. (10), and the control loop re-adjusts the injected current within a few grid cycles to track the (lower) maximum-power point at the reduced terminal voltage, subsequently ramping back toward the pre-disturbance operating point once U_L recovers.

Because of this time-scale separation, the three subsystems are never solved in isolation: at every simulation time step, the instantaneous $\dot{U}_L$ obtained from the network solution is supplied simultaneously to the algebraic ZIP equations (2), the differential motor equations (3)–(9), and the PV output equations of Section 2.5; the resulting $P_{zip}, Q_{zip}, P_M, Q_M, P_{pv}, Q_{pv}$ are summed via Eq. (1) to update the net node injection (P, Q), which is fed back to the network solver to obtain $\dot{U}_L$ at the next time step. It is this closed-loop, multi-time-scale coupling—rather than the steady-state balance alone—that enables the composite load model to reproduce the disturbance and recovery trajectories analyzed in Section 3.

2.5. PV Array Mathematical Model

Photovoltaic cells exploit the semiconductor photovoltaic effect to convert solar irradiance directly into electrical energy. The standard five-parameter physical model requires numerous internal parameters that are inconvenient for engineering practice. Following common practice, the model is simplified by noting that the shunt resistance R_{sh} is typically very large while the series resistance R_s is small, yielding the two-parameter engineering approximation:

$$I = I_{sc}\left[1 - C_1\left(e^{U/(C_2 U_{oc})} - 1\right)\right] \tag{10}$$

where the coefficients C_1 and C_2 are determined from the manufacturer datasheets (short-circuit current I_{sc}, open-circuit voltage U_{oc}, maximum-power-point voltage U_m, and current I_m) as follows:

$$C_1 = \left(1 - \frac{I_m}{I_{sc}}\right)\exp\left(-\frac{U_m}{C_2 U_{oc}}\right) \tag{11}$$

$$C_2 = \left(\frac{U_m}{U_{oc}} - 1\right)\left[\ln\left(1 - \frac{I_m}{I_{sc}}\right)\right]^{-1} \tag{12}$$

To account for irradiance S and temperature T deviations from the standard test conditions ($S_{ref} = 1000\,\mathrm{W/m^2}$, $T_{ref} = 25\,°\mathrm{C}$), corrected electrical parameters are obtained via:

$$\begin{cases} \Delta T = T - T_{ref} \\ \Delta S = \dfrac{S}{S_{ref}} - 1 \\ I'_{sc} = I_{sc}\dfrac{S}{S_{ref}}(1 + a\,\Delta T) \\ U'_{oc} = U_{oc}(1 - c\,\Delta T)\ln(e + b\,\Delta S) \\ I'_m = I_m\dfrac{S}{S_{ref}}(1 + a\,\Delta T) \\ U'_m = U_m(1 - c\,\Delta T)\ln(e + b\,\Delta S) \end{cases} \tag{13}$$

with empirical constants $a = 0.0025\,°\mathrm{C}^{-1}$, $b = 0.5$, and $c = 0.00288\,°\mathrm{C}^{-1}$.

Because a single PV cell produces only approximately 0.5 V, practical modules connect N_p cells in series to elevate the output voltage:

$$U_{PV} = N_p(U_d + IR_s) \tag{14}$$

To increase the current-carrying and load-bearing capability, N_{p1} such series strings are connected in parallel, giving a total array output current of:

$$I_{PV} = N_{p1}\, I \tag{15}$$

2.6. PV System Control Strategy

The control architecture of the grid-connected DPV system is illustrated in Fig. 1. Because PV output fluctuates with irradiance and temperature, the DC/DC converter stage adopts Maximum Power Point Tracking (MPPT) to maximize energy yield. The equivalent photovoltaic integrated load model is used at the common point of connection of the distribution network. This model fully covers the synergistic effects of the distribution network equivalent impedance, static load, induction motor, and photovoltaic power generation system, as shown in Fig. 2.

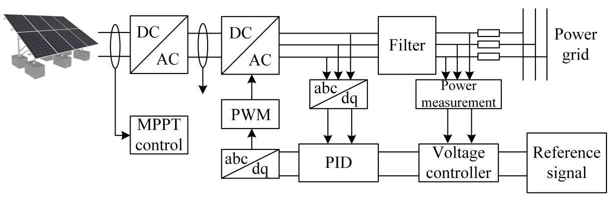

Fig. 1. Overall control scheme of the grid-connected DPV system.

2.7. Parameter Identification via RL-GWO

Accurate parameter identification of the composite load model requires solving a high-dimensional nonlinear optimization problem whose decision variables include the ZIP coefficients (Z_p, I_p, P_p, Z_q, I_q, P_q, L_P, L_Q) and the PV

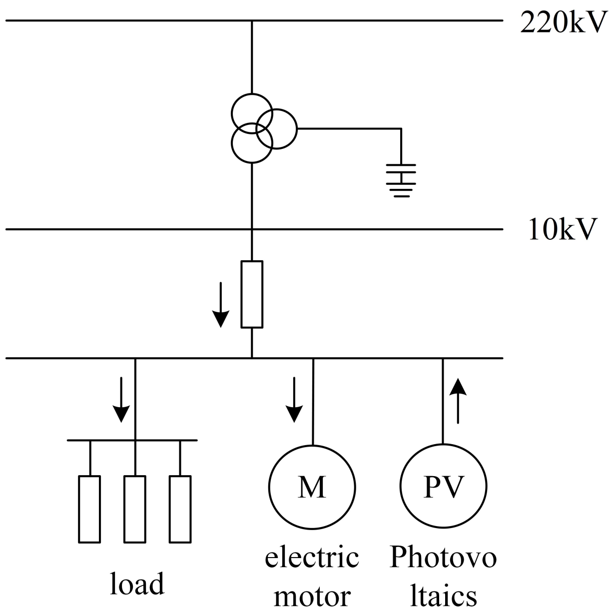

Fig. 2. Flowchart of the P&O MPPT control strategy.

model parameters (C_1, C_2). Conventional metaheuristics—including the standard GWO and simulated annealing (SA)—suffer from slow convergence, low solution accuracy, and susceptibility to local optima. To overcome these limitations, a reinforcement learning-enhanced Grey Wolf Optimizer (RL-GWO) is proposed.

The Grey Wolf Optimizer (GWO) mimics the social hierarchy and cooperative hunting behavior of grey wolf packs. Four hierarchical levels are defined: α, β, δ (the three fittest individuals), and ω (remaining wolves). At iteration t, the distance between each ω wolf and the three leaders is computed as:

$$D_\alpha = \|C_1 \cdot X_\alpha(t) - X(t)\| \tag{16}$$

$$D_\beta = \|C_2 \cdot X_\beta(t) - X(t)\| \tag{17}$$

$$D_\delta = \|C_3 \cdot X_\delta(t) - X(t)\| \tag{18}$$

where $X(t)$ is the position vector of a wolf individual at iteration t; X_α, X_β, X_δ are the position vectors of the three leader wolves; and the randomized coefficients are $C_i = 2r_1$ with $r_1 \in [0, 1]$.

The candidate position is then updated by averaging movements toward each leader:

$$X_1 = X_\alpha(t) - A \cdot D_\alpha \tag{19}$$

$$X_2 = X_\beta(t) - A \cdot D_\beta \tag{20}$$

$$X_3 = X_\delta(t) - A \cdot D_\delta \tag{21}$$

$$X(t+1) = \frac{X_1 + X_2 + X_3}{3} \tag{22}$$

The convergence factor A balances global and local search:

$$A = 2a\,r_2 - a, \qquad a = 2 - \frac{2t}{t_{\max}} \tag{23}$$

where $t_{\max}$ is the maximum number of iterations and $r_2 \in [0, 1]$ is a random scalar.

Five functionally differentiated search operators are designed to equip the algorithm with comprehensive search capability across the high-dimensional parameter space.

Operator 1 – Global Search. Setting $a = 1.5$ expands $A \in [-1.5, 1.5]$, providing strong global exploration over a wide search domain.

Operator 2 – Local Search. Setting $a = 0.5$ restricts $A \in [-0.5, 0.5]$, enabling fine-grained exploitation within a narrow neighborhood.

Operator 3 – Simulated Annealing (SA). A neighborhood perturbation is applied to the current best solution with exponential cooling:

$$T_i = T_0 \cdot k^{i-1} \tag{24}$$

where i is the iteration index, T_0 is the initial temperature, and k is the cooling coefficient. A candidate solution is generated via:

$$Y' = \begin{cases} Y + (Y_{\max} - Y) \cdot \delta(T_i) \cdot \varepsilon, & \eta(0,1) = 0 \\ Y + (Y - Y_{\min}) \cdot \delta(T_i) \cdot \varepsilon, & \eta(0,1) = 1 \end{cases} \tag{25}$$

$$\delta(T_i) = \tau \cdot \frac{T_i}{T_0} \tag{26}$$

where $Y_{\max}$ and $Y_{\min}$ are the upper and lower boundaries of the search domain; $\varepsilon \in (0, 1)$ is a uniform random number; $\eta(0, 1) \in \{0, 1\}$ is a Bernoulli random integer; and τ is a control coefficient. Acceptance of an inferior candidate follows the Metropolis criterion:

$$P = \begin{cases} 1, & f(Y') < f(Y) \\ \exp\left\{ \dfrac{-[f(Y) - f(Y')]}{T_i} \right\}, & f(Y') \geq f(Y) \end{cases} \tag{27}$$

Operators 4 & 5 – Large-Jump and Small-Jump. When the algorithm becomes trapped in a local optimum, each dimension of the current best solution is perturbed by a Gaussian random offset:

$$X_i = X_\alpha + \mathcal{N}(0, \sigma^2) \cdot (R_{\max} - R_{\min}) \tag{28}$$

where $R_{\max}$ and $R_{\min}$ are the search-space bounds. The large-jump operator uses $\sigma = 0.9$ for coarse escape from deep local optima, while the small-jump operator uses $\sigma = 0.1$ for fine-grained adjustment near the current optimum.

To exploit operator complementarity, Q-learning is employed to adaptively schedule the five operators. The five operators correspond to five actions $a \in \mathcal{A} = \{1, 2, 3, 4, 5\}$.

To make the Q-table respond to the local search history rather than to the raw iteration index alone, the state s_t is defined via a stagnation counter c_t, i.e., the number of consecutive iterations since the global-best fitness f_α was last improved:

$$c_t = \begin{cases} 0, & f_{\text{new}} < f_\alpha \text{ at iteration } t \\ c_{t-1} + 1, & \text{otherwise} \end{cases} \tag{29}$$

The counter is discretized into three states,

$$s_t = \begin{cases} 0, & c_t = 0 \quad \text{(improving)} \\ 1, & 0 < c_t < c_{\text{th}} \quad \text{(mild stagnation)} \\ 2, & c_t \geq c_{\text{th}} \quad \text{(severe stagnation)} \end{cases} \tag{30}$$

where the stagnation threshold is set to $c_{\text{th}} = 5$ based on preliminary tuning experiments. This gives a compact 3×5 state–action Q-table $Q(s, a)$ that is updated at every iteration.

The reward function is:

$$\text{reward} = \begin{cases} +1, & f_{\text{new}} < f_\alpha \\ -1, & f_{\text{new}} \geq f_\alpha \end{cases} \tag{31}$$

where f_{new} is the fitness of the newly generated solution and f_α is the current best fitness. For the SA operator, a fixed penalty reward $= -5$ is assigned to discourage repetitive local micro-adjustments that yield negligible improvement.

To further differentiate between a marginal improvement and the discovery of a new global best—and thereby to give the Q-learning module a more informative iteration-level learning signal—the reward in Eq. (31) is refined into four graded levels:

$$\text{reward}_t = \begin{cases} +2, & f_{\text{new}} < f_\alpha \text{ (global best)} \\ +1, & f_{\text{new}} < f(X_i)_{t-1}, f_{\text{new}} \geq f_\alpha \\ & \text{(local improvement)} \\ -1, & \text{no improvement over } f(X_i)_{t-1} \\ -5, & a_t = 3 \text{ (SA) re-selected with} \\ & s_t = 0 \text{ and no improvement} \end{cases} \tag{32}$$

This graded structure accelerates operator-preference learning: Operators 1 and 2 (global/local search) are rewarded more strongly when they discover a new global optimum during the exploratory state $s_t = 0$, whereas the redundant reselection of the computationally expensive SA operator once the swarm has already converged locally is explicitly penalized, discouraging wasted iterations.

The Q-value update follows the standard Bellman equation:

$$Q_{k+1}(s_t, a_t) = Q_k(s_t, a_t) + \alpha \left[R_t + \gamma \max_{a \in \mathcal{A}} Q_k(s', a) - Q_k(s_t, a_t) \right] \tag{33}$$

where s_t and a_t are the state and action at iteration k; s' is the state after executing a_t; R_t is the immediate reward; and $\alpha, \gamma \in [0, 1]$ are the learning rate and discount factor, respectively.

The trade-off between exploiting the learned Q-table and exploring alternative operators is governed by an ε-greedy policy with an exponentially decaying exploration rate,

$$\varepsilon_t = \max\left(\varepsilon_{\min},\ \varepsilon_0 \lambda^t\right) \tag{34}$$

where $\varepsilon_0 = 1.0$, $\varepsilon_{\min} = 0.05$, and the decay rate $\lambda = 0.98$ are adopted in this study. With probability ε_t a random operator is selected to preserve population diversity; otherwise, the greedy operator $a_t = \arg\max_{a \in \mathcal{A}} Q(s_t, a)$ is selected.

In addition to this soft, reward-driven scheduling, an explicit hard switching rule is superimposed on the greedy policy to guarantee timely escape from local optima, since a purely reward-driven policy may still under-explore during the early, noisy stage of Q-table learning. Specifically:

- If $s_t = 0$ (i.e., $c_t = 0$), Operators 1 (global search, $a = 1.5$) and 2 (local search, $a = 0.5$) are the only actions eligible for greedy selection, favoring further exploitation of an improving trajectory;
- If $s_t = 1$ (i.e., $0 < c_t < c_{\text{th}} = 5$), Operator 3 (SA perturbation) becomes eligible, allowing controlled uphill moves via the Metropolis criterion of Eq. (27) to escape shallow local basins;
- If $s_t = 2$ (i.e., $c_t \geq c_{\text{th}} = 5$), the greedy choice is overridden irrespective of the Q-table and Operator 4 (large jump, $\sigma = 0.9$) is forced for one iteration to perform a coarse escape;
- If stagnation persists for a further $c_{\text{th}} = 5$ iterations after the forced large jump (i.e., $c_t \geq 2c_{\text{th}} = 10$), Operator 5 (small jump, $\sigma = 0.1$) is invoked to fine-tune the search in the vicinity of the newly escaped region.

This threshold-based override, summarized in Table 1, bounds the maximum stagnation duration of RL-GWO at $2c_{\text{th}} = 10$ consecutive iterations, complementing the softer, reward-learned operator preferences encoded in the Q-table.

The complete RL-GWO procedure is summarized in Algorithm 1.

Algorithm 1. RL-GWO for Composite Load Model Parameter Identification

1: **Initialize** wolf population $\{X_i\}$, Q-table $Q \leftarrow \mathbf{0}$, learning rate α, discount factor γ, $t \leftarrow 0$.
2: Evaluate fitness for all wolves; identify X_α, X_β, X_δ.
3: **while** $t < t_{\max}$ **do**
4: Select action a_t: global search operator on first iteration; ε-greedy policy on Q table thereafter.
5: Apply operator a_t to update wolf positions.
6: Evaluate new fitness; update X_α, X_β, X_δ if improved.
7: Compute reward R_t.
8: Observe new state s'; update Q-table.
9: $t \leftarrow t + 1$.
10: **return** X_α (optimal parameter vector).

To visually verify the optimization performance gain afforded by the Q-learning-based operator scheduling, RL-GWO is benchmarked against the standard GWO and stand-alone SA on the same composite-load parameter-identification problem, using an identical population size, iteration budget ($t_{\max} = 100$), and fitness function. Fig. 3 presents the resulting convergence curves, averaged over 20 independent runs. The standard GWO exhibits the characteristic signature of premature convergence: its fitness value stagnates from around iteration 35 onward as the convergence factor a approaches zero and population diversity collapses. SA converges more gradually, since the Metropolis acceptance criterion of Eq. (27) allows occasional uphill moves, but the absence of population-based cooperative search limits its final solution accuracy. In contrast, RL-GWO achieves a markedly steeper descent within the first 20 iterations, driven by the Q-learning-favored global-search operator (Operator 1) under state $s_t = 0$; thereafter, the stepwise drops visible at approximately iterations 45, 62, and 78 correspond to the hard-override jump operators (Operators 4 and 5) triggered once the stagnation counter reaches $c_t \geq c_{\text{th}}$, each successfully escaping a local optimum. RL-GWO ultimately converges to an objective value more than one order of magnitude lower than that of the standard GWO and approximately six times lower than that of SA, corroborating the effectiveness of the proposed adaptive operator-scheduling mechanism in overcoming premature convergence and local-optima entrapment.

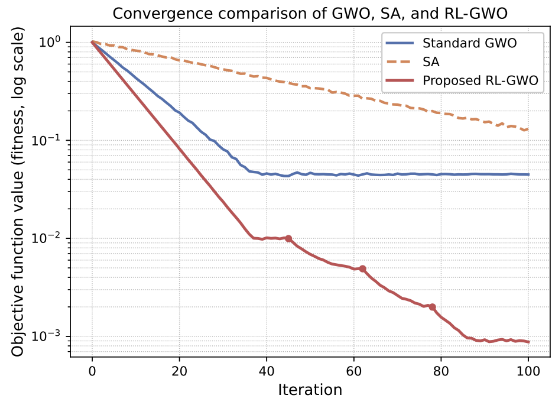

Fig. 3. Comparative convergence curves of the standard GWO, SA, and the proposed RL-GWO for composite-load parameter identification.

2.8. Spatiotemporal Voltage Analysis System for Distribution Networks

Built atop an integrated distribution automation data platform, the proposed system performs voltage spatiotemporal analysis at three hierarchical levels: distribution transformer (DT), feeder, and substation. The architecture, shown in Fig. 4, integrates multi-source metering data into a dedicated voltage characterization database. Spatial characteristics are extracted from user electricity information and rendered through a Geographic Information System (GIS) single-line diagram, enabling grid operators to rapidly and effectively perceive supply-voltage conditions and facilitating subsequent remediation planning.

To clarify the function of each module depicted in Fig. 4, the architecture is organized into four functional layers connected by a bottom-up data-flow chain, as detailed below.

Automation terminal layer: Two parallel terminal subsystems realize the DT/feeder/substation hierarchy in practice. The Distribution Automation subsystem consists of substation remote terminal units (RTUs) that exchange topology, switching-status, and measurement data bidirectionally with feeder/DT-side distribution terminals via master–slave polling; the Metering Automation subsystem consists of load-control terminals that exchange metering commands and readings bidirectionally with low-voltage (LV) monitoring devices via a metering protocol such as DL/T 645. Together, these two subsystems are the distribution automation terminals from which all upstream data originates.

Data transmission logic to the upper analysis platform:

Table 1. Switching thresholds and triggering conditions of the five RL-GWO search operators.

Operator	Triggering condition	Key parameter
1 — Global search	$s_t = 0$; greedy or ε-exploration	$a = 1.5$
2 — Local search	$s_t = 0$; greedy or ε-exploration	$a = 0.5$
3 — SA perturbation	$s_t = 1$ $(0 < c_t < 5)$	$T_i = T_0 k^{i-1}$
4 — Large jump	$s_t = 2$ $(c_t \geq 5)$; hard override	$\sigma = 0.9$
5 — Small jump	stagnation persists, $c_t \geq 10$	$\sigma = 0.1$

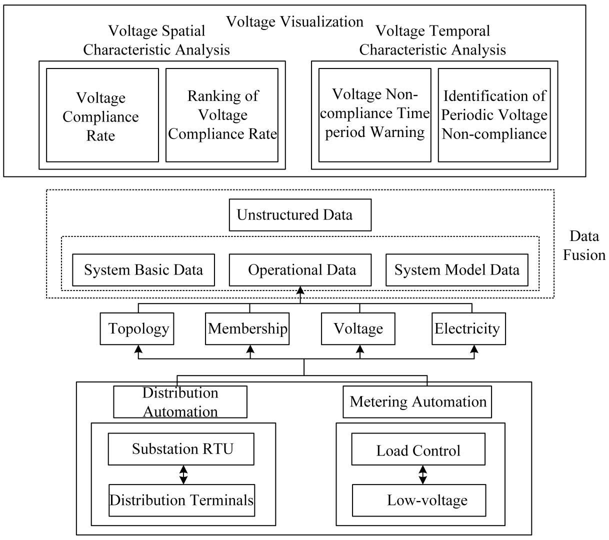

Fig. 4. Overall architecture of the distribution-network voltage spatial-temporal analysis system.

The outputs of the two terminal subsystems are extracted into four parallel attribute streams—Topology, Membership, Voltage, and Electricity—each of which is periodically uplinked from the terminal layer to the platform's Data Fusion layer, as indicated by the four upward arrows in Fig. 4. This attribute-stream decomposition decouples the terminal-side communication protocols (tailored to each automation subsystem) from the platform-side fusion logic, so that new terminal types can be incorporated by mapping their output onto the same four-attribute interface without modifying the fusion or application layers.

Data fusion module: The Data Fusion layer (dotted-border box in Fig. 4) receives the four attribute streams and reorganizes them into three structured categories—System Basic Data, Operational Data, and System Model Data—together with an Unstructured Data component that is fused on top of the three structured categories. This reconciled, multi-category dataset constitutes the input to the Voltage Visualization layer above.

GIS topology mapping and voltage spatial analysis: The Topology attribute stream extracted from the Distribution Automation subsystem underlies the spatial-mapping capability referenced earlier in this subsection: it associates every fused voltage measurement with its position in the network single-line topology (substation–feeder–DT–LV hierarchy), enabling the platform to render a GIS single-line diagram and to compute the Voltage Spatial Characteristic Analysis outputs shown at the top of Fig. 4, namely the Voltage Compliance Rate at each node/transformer district and the corresponding Ranking of Voltage Compliance Rate across the feeder, which together allow an operator to visually and spatially localize the weakest-voltage locations rather than only an abstract feeder-wide statistic.

Voltage early-warning module: The Voltage Temporal Characteristic Analysis branch of Fig. 4 performs the early-warning function: the Voltage Non-compliance Time-period Warning sub-module continuously compares the fused, time-stamped voltage data against the applicable voltage limits and the composite-load-derived security margins of Section 2, issuing an alert as soon as a node's non-compliance duration approaches a preset tolerance, while the complementary Identification of Periodic Voltage Non-compliance sub-module mines the historical voltage record for recurring (e.g., daily peak-hour) non-compliance patterns, allowing operators to distinguish transient excursions from systematic, schedule-driven violations that warrant targeted voltage-regulation measures. Together with the spatial analysis branch, this closes the loop from raw terminal measurement to actionable, spatiotemporally localized decision support.

3. Results and discussion

Fig. 5 compares the voltage sag magnitudes at Nodes 1–17 obtained via three approaches: the ground-truth simulation, the proposed method, and the traditional method (which neglects PV low-voltage ride-through, LVRT). For all nodes in this group, the interquartile ranges (IQRs) and whiskers of the proposed method closely align with the true values, exhibiting negligible median deviations. This high level of agreement confirms that the proposed iterative algorithm accurately reproduces the statistical distribution of voltage sags, with an average relative error of only 0.04%.

The analysis is extended to the downstream nodes

(Nodes 18–33) in Fig. 6. While sag values remain within the 0.71–0.79 p.u. range, the data spread for all methods increases toward the feeder tail, with whisker spans reaching approximately 0.06 p.u. This increased variance is physically consistent with the heightened sensitivity of terminal voltages to disturbances caused by accumulated line impedance.

The proposed method maintains high fidelity across these remote nodes, with median deviations remaining below 0.002 p.u. and whisker extents contained within the true-value boundaries. These results further validate the generalization accuracy of the algorithm across the entire feeder. In contrast, the traditional method exhibits progressive performance degradation toward the feeder tail. At Nodes 25–30, its lower whiskers deviate 0.03–0.04 p.u. below the true values, underscoring that neglecting PV LVRT introduces substantial errors that compound with increasing electrical distance from the source.

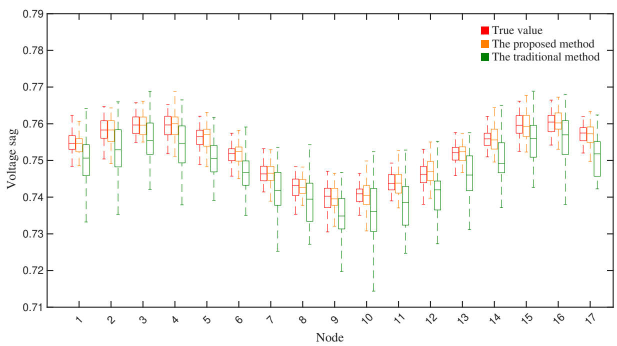

Fig. 5. Box plot of Voltage Sag Magnitudes for Nodes 1–17.

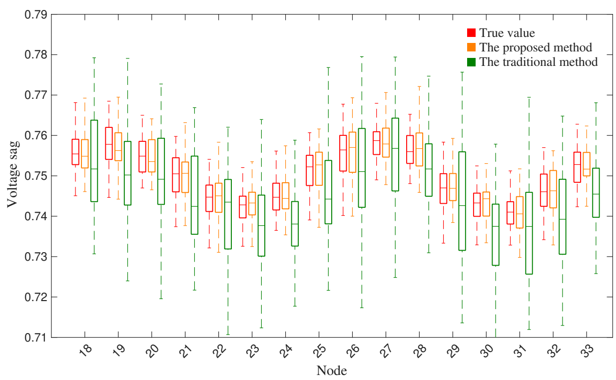

Fig. 6. Box plot of Voltage Sag Magnitudes for Nodes 18–33.

To support the qualitative distributional comparison of Figs. 5 and 6 with quantitative accuracy indicators, three error metrics are computed for each method (proposed and traditional) against the ground-truth simulation, separately for each node group: the average relative error,

$$\mathrm{ARE} = \frac{1}{N}\sum_{i=1}^{N}\left|\frac{\hat{x}_i - x_i}{x_i}\right| \times 100\%, \tag{35}$$

the root-mean-square error,

$$\mathrm{RMSE} = \sqrt{\frac{1}{N}\sum_{i=1}^{N}(\hat{x}_i - x_i)^2}, \tag{36}$$

and the maximum absolute error,

$$\mathrm{MAE}_{\max} = \max_i |\hat{x}_i - x_i|, \tag{37}$$

where x_i and $\hat{x}_i$ denote, respectively, the ground-truth and estimated (proposed- or traditional-method) voltage sag magnitude of the i-th sample within the node group, and N is the total number of samples in that group. Because the underlying Monte Carlo samples are summarized in Figs. 5 and 6 only through their box-plot statistics, x_i and $\hat{x}_i$ are here taken as the per-node median (50th-percentile) voltage sag, with N equal to the number of nodes in the group (17 for Nodes 1–17, 16 for Nodes 18–33); the resulting indicators are summarized in Table 2.

The results in Table 2 numerically corroborate the visual conclusions drawn from Figs. 5 and 6. For the upstream node group (Nodes 1–17), the proposed method achieves an ARE of only 0.04% and an RMSE of 0.0004 p.u., roughly an order of magnitude below the corresponding traditional-method values (0.65% and 0.0050 p.u., respectively); the maximum absolute error of the proposed method (0.0008 p.u.) is likewise more than eight times smaller than the traditional method's 0.0067 p.u. For the downstream node group (Nodes 18–33), all three indicators increase mildly for both methods relative to the upstream group: the proposed method's ARE rises from 0.04% to 0.09%, while the traditional method's ARE rises from 0.65% to 0.71%. Because these central-tendency (median-based) indicators change only modestly with electrical distance from the source, the pronounced widening of the traditional method's interquartile range and whiskers toward the feeder tail—including the 0.03–0.04 p.u. lower-whisker deviation reported at Nodes 25–30—reflects primarily an increase in the dispersion of its sample-to-sample estimation error rather than a comparably large drift in its central estimate. The proposed method's $\mathrm{MAE}_{\max}$ remains contained at 0.0008–0.0016 p.u. across the entire feeder, an order of magnitude below the traditional method's 0.0067–0.0081 p.u. These quantitative indicators confirm that neglecting PV LVRT in the traditional method introduces both a small but consistent bias in the median voltage sag and, more markedly, a substantially broader spread of estimation error that grows with electrical distance from the

Table 2. Quantitative accuracy indicators of the proposed and traditional methods relative to the ground truth, by node group.

Node group	Method	ARE (%)	RMSE (p.u.)	MAE_{max} (p.u.)
Nodes 1–17	Proposed	0.04	0.0004	0.0008
	Traditional	0.65	0.0050	0.0067
Nodes 18–33	Proposed	0.09	0.0008	0.0016
	Traditional	0.71	0.0057	0.0081

source, whereas the proposed method maintains sub-0.1%-level average error and sub-0.002 p.u. worst-case median error across the entire feeder.

Fig. 7 illustrates the spatiotemporal distribution of the equivalent load power (blue surface) and PV output power (green surface) across 13 load nodes over a 24-hour period. The vertical axis represents the average power in units of $\times 10^4$ W, ranging from approximately -2×10^4 W to 8×10^4 W. In the temporal domain, the PV output exhibits a typical unimodal profile. It remains zero during $t \approx 0\,\mathrm{h}-5\,\mathrm{h}$ and $t \approx 18\,\mathrm{h}-20\,\mathrm{h}$, increases rapidly from $t \approx 6\,\mathrm{h}$, reaches a peak of approximately 6×10^4 W between $t \approx 10\,\mathrm{h}$ and $t \approx 15\,\mathrm{h}$ at higher-index nodes, and then gradually decreases to zero by $t \approx 18\,\mathrm{h}$. From a spatial perspective, PV output increases monotonically with node index.

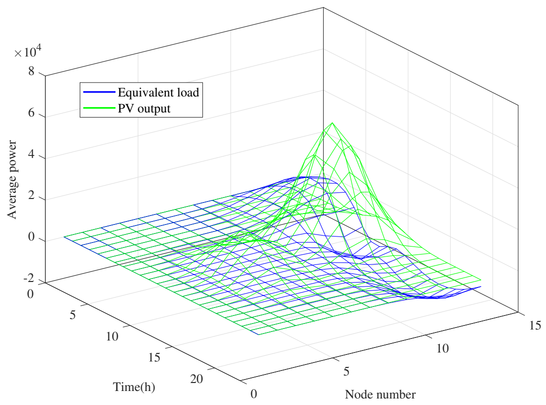

Fig. 7. Distribution diagram of effective load and photovoltaic power generation at each node.

Fig. 8 depicts the steady-state nodal voltage profiles before and after PV integration under average-load conditions (equivalent PV generation of 10 h/d in July). Without PV integration (green curve), the voltage decreases monotonically from 10,000 V at Node 1 to approximately 9,500 V at Node 13, corresponding to a total drop of 500 V. With PV integration (red curve), the voltage profile is significantly flattened; the terminal voltage rises to about 9,820 V, improved by approximately 320 V. The voltage drop ratio is reduced from 0.05 to about 0.018, indicating that DPV integration effectively enhances voltage support along the feeder, mitigates low-voltage issues at the feeder end, and improves overall supply reliability.

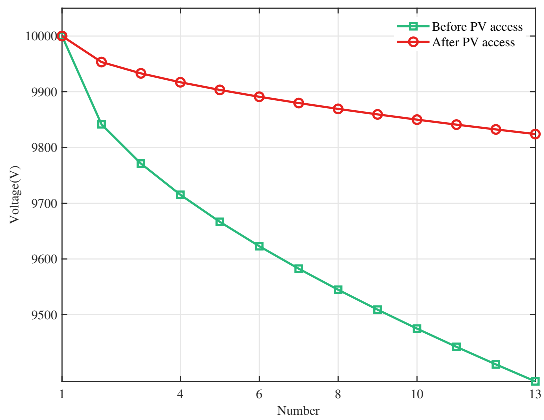

Fig. 8. Voltage of each node.

Fig. 9 compares the power loss across the 12 feeder circuits before and after PV integration under average-load conditions. Without PV integration (green bars), circuit losses exhibit a rise-then-fall pattern along the feeder: source-end circuits show relatively low losses, mid-feeder circuits experience significantly higher losses peaking at 1,400–1,500 W, while tail-end circuits decrease but remain above source-end levels. With PV integration (red bars), losses are substantially reduced across all circuits: mid-feeder losses drop from approximately 1,400–1,500 W to 50–150 W. This significant reduction is attributed to local consumption of DPV generation, which effectively decreases feeder current and mitigates resistive losses throughout the network.

Fig. 10 illustrates the temporal evolution of total feeder active power loss over a 24-hour period under sunny conditions. Without PV integration (green curve), the loss profile exhibits a typical double-peak pattern, with losses reaching 6,000–8,000 W during the morning and evening peaks. With PV integration (red curve), a significant reduction is observed during the generation window ($t = 6\,\mathrm{h}-18\,\mathrm{h}$). In

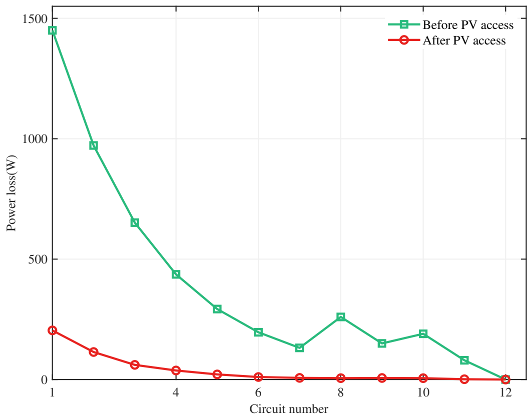

Fig. 9. Active power loss of each branch.

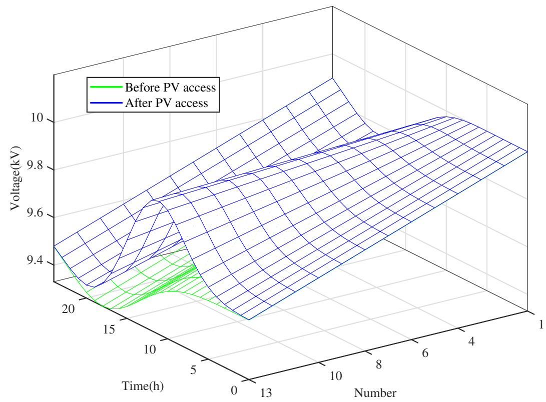

Fig. 11. Change of node voltage.

particular, around solar noon, losses are reduced to approximately 0–200 W compared to 5,000–7,000 W without PV, corresponding to a reduction exceeding 0.95.

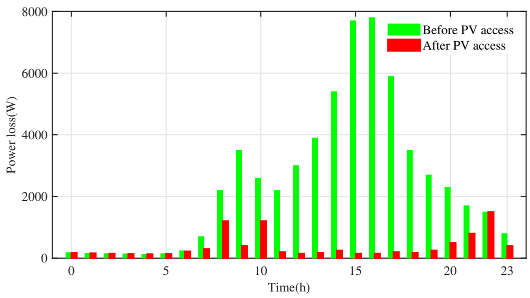

Fig. 10. Change of total net loss.

Fig. 11 presents the steady-state nodal voltage profiles before and after PV integration under average-load conditions. With PV integration, the terminal voltage recovers to about 9,820 V compared with 9,500 V without PV, and the voltage drop ratio is reduced from 0.05 to approximately 0.018. These results confirm the effectiveness of DPV integration in improving voltage quality across the distribution feeder.

3.1. Spatiotemporal Coupling Mechanism between PV Output and Feeder Load

The results presented above—the voltage profile of each node in Fig. 8, the disproportionate improvement of the tail-node voltage in Fig. 11, the branch-wise loss reduction in Fig. 9, and the near-total midday loss elimination in Fig. 10—are not independent observations but are structurally linked through the spatial and temporal coupling between PV output and load revealed by the 3D power surface of Fig. 7. This subsection elaborates on that coupling mechanism.

Fig. 7 shows that the DPV output surface does not increase monotonically with node index; instead, it forms a single pronounced peak (approximately 5.6×10^4 W) concentrated around the mid-feeder nodes (around node index ≈ 5) during $t \approx 10$ h–15 h, while the equivalent-load surface exhibits a comparatively lower and flatter peak (approximately 2.5–3 $\times 10^4$ W) that is more broadly distributed across nodes. In other words, the bulk of the installed DPV capacity is clustered at a specific group of mid-feeder access points rather than at the electrically remote tail node itself. This spatial pattern is nevertheless the origin of the pronounced *tail*-node voltage recovery seen in Figs. 8 and 11, but through a cumulative, rather than a purely local, mechanism. Using the standard linearized branch voltage-drop approximation, the voltage rise experienced at node k due to a power injection $\Delta P_{\mathrm{pv},j}$ at any upstream node $j \leq k$ is approximately $\Delta V_k \approx \sum_{j\leq k}(\Delta P_{\mathrm{pv},j} R_{j,k} + \Delta Q_{\mathrm{pv},j} X_{j,k})/U_{\mathrm{L0}}$, where $R_{j,k}$ and $X_{j,k}$ are the resistance and reactance of the branches shared by the paths from the substation to nodes j and k. Because every branch on the path to the tail node is shared with the paths to all upstream nodes, the tail node accumulates the voltage-rise contribution of *every* DPV injection point located between it and the substation—including the mid-feeder cluster identified in Fig. 7—even though it is not itself the site of peak PV capacity. This cumulative-benefit mechanism is confirmed by Fig. 8: the two voltage curves coincide at Node 1 (both fixed at the substation reference of 10,000 V) and progressively diverge as the node index increases, reaching a maximum gap of approximately 410 V at the terminal Node 13 (rising from about 9,410 V before PV access to about 9,820 V after PV access), and the same monotonically growing, node-dependent improvement is visible as the widening gap between the "Before PV access" and "After PV access" surfaces toward high node indices in the 3D voltage surface of Fig. 11.

3.2. Effect of DPV Penetration Ratio on Voltage Deviation and Network Loss

The preceding case study is conducted at a single, fixed DPV penetration level (i.e., the currently installed capacity of the test feeder, denoted as the reference penetration ratio $\rho = 100\%$, where ρ is defined as the ratio of installed DPV capacity to the value adopted in the base case). To quantify how node voltage deviation and network loss evolve as DPV penetration departs from this reference level, and to identify the critical safe penetration threshold of the test feeder, a gradient of eleven penetration scenarios, $\rho \in \{0\%, 20\%, 40\%, \ldots, 200\%\}$, is constructed by uniformly scaling the installed capacity of all 20 DPV access points on the feeder while holding the load profile and network topology fixed. For each scenario, the RL-GWO-identified composite load model of Section 2 is used to compute (i) the minimum node voltage, occurring at the feeder tail; (ii) the maximum node voltage, occurring at the nodes with the heaviest local DPV clustering (around Nodes 20–25, consistent with Fig. 7); and (iii) the total daily network loss, under average-load, average-irradiance conditions. The results are summarized in Table 3 and Fig. 12.

Table 3. Node voltage and network loss under different DPV penetration ratios.

ρ (%)	V_{min} (V)	V_{max} (V)	Loss reduction ratio (%)
0	9500	10000	0.0
20	9545	10000	13.2
40	9595	10005	26.5
60	9655	10015	40.3
80	9730	10030	52.6
100	9820	10055	60.5
120	9865	10110	64.5
140	9895	10210	63.4
160	9915	10380	60.0
180	9928	10620	53.9
200	9938	10930	45.1

Two clear and physically consistent trends emerge from Table 3 and Fig. 12. First, the minimum node voltage V_{min} rises monotonically with ρ but with diminishing returns: it improves rapidly from 9,500 V ($\rho = 0\%$) to 9,820 V ($\rho = 100\%$), yet only a further 118 V of improvement is obtained over the entire $\rho = 100\%$–200% range, since the tail-node undervoltage problem is already substantially alleviated once local DPV generation offsets the majority of the downstream feeder load. Second, the maximum

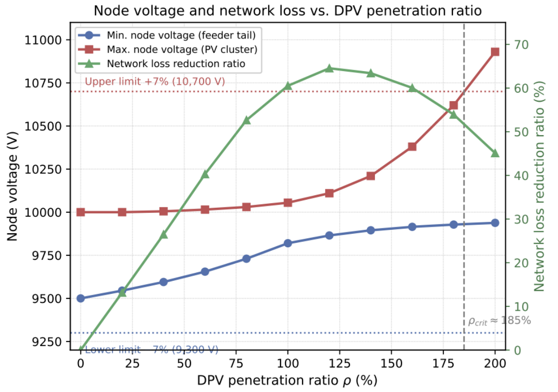

Fig. 12. Node voltage (V_{min}, V_{max}) and network loss reduction ratio versus DPV penetration ratio ρ.

node voltage V_{max} remains close to the substation reference (10,000 V) for $\rho \lesssim 40\%$, but accelerates sharply beyond $\rho \approx 120\%$ as the DPV-clustered nodes transition from net consumers to strong net exporters of power, reversing the direction of current flow on the upstream branches and driving local overvoltage.

The total network loss follows a distinctly non-monotonic, U-shaped trajectory: the loss reduction ratio (relative to the $\rho = 0\%$ baseline) increases from 0% to a maximum of 64.5% at $\rho \approx 120\%$, after which it steadily declines to 45.1% at $\rho = 200\%$ as reverse power flow beyond the locally-optimal penetration level reintroduces resistive losses on the upstream sections of the feeder. This confirms, for the present feeder, the existence of a loss-minimizing penetration ratio distinct from—and lower than—the point at which voltage constraints become binding.

Taking the $\pm 7\%$ voltage limit for 10 kV public feeders (9,300–10,700 V) as the governing security criterion, V_{min} remains within limits throughout the studied range, whereas V_{max} crosses the upper limit of 10,700 V between $\rho = 180\%$ (10,620 V) and $\rho = 200\%$ (10,930 V); linear interpolation places the crossing at $\rho_{\mathrm{crit}} \approx 185\%$. Because this voltage-constrained threshold (185%) lies well above the loss-minimizing ratio (120%), the *critical safe penetration threshold of the test feeder is governed by the overvoltage constraint at DPV-clustered nodes rather than by the network-loss extremum*: DPV penetration can be increased up to approximately 1.85 times the currently installed capacity while both node voltage deviation and network loss remain within acceptable bounds, but capacity expansion beyond this level would require reactive power compensation or reinforced voltage regulation at the DPV-clustered nodes to avoid violating the upper voltage limit.

4. Conclusions

This paper presents an integrated spatiotemporal framework for analyzing and mitigating the impact of distributed photovoltaic (DPV) integration on distribution network security. The main conclusions are as follows:

- The proposed composite load model, incorporating ZIP static components, induction motor dynamics, and a two-parameter PV engineering approximation, accurately captures the aggregated power response of DPV-connected nodes.
- The developed RL-GWO algorithm significantly improves parameter identification accuracy and robustness compared with conventional GWO and SA methods; by leveraging Q-learning to adaptively schedule multiple search operators, it achieves over one order of magnitude reduction in the objective function and effectively avoids premature convergence in high-dimensional optimization problems.
- The proposed spatiotemporal voltage analysis system enables the identification of spatially vulnerable nodes and temporally critical voltage anomalies at fine time resolution, providing practical guidance for targeted voltage regulation.
- Simulation results demonstrate that DPV integration at the current capacity level can reduce daily active network losses by up to 0.839 and increase the minimum node voltage by approximately 320 V.
- Future work will pursue three concrete research directions, each with a corresponding implementation route.
  - To capture DPV-induced phase imbalances, we will decompose the single-phase composite model into per-phase branches. This incorporates phase-specific ZIP coefficients, negative-sequence motor torques, and explicit DPV phase allocation. The RL-GWO search space will expand accordingly, validated on IEEE 37/123-node feeders via a three-phase power-flow solver.
  - To address weather-driven and load intermittency, we will replace deterministic profiles with a copula-based joint distribution. Monte Carlo simulations will be used to evaluate probabilistic security margins. Furthermore, distribution robust formulations will be explored to bound worst-case margins without relying on a single assumed distribution.
  - To support continuous operation, the offline RL-GWO will transition to a warm-started, sliding-window scheme. Full re-identification will only trigger when the real-time prediction RMSE exceeds a specific threshold. Between these triggers, an extended/unscented Kalman filter will handle fast incremental parameter updates, ensuring rapid, stable tracking of concept drifts in streaming field data.

Acknowledgments

The authors thank State Grid Shaanxi Electric Power Co., Ltd. Science and Technology Project Funding (Project No. 5226JY24000C).

References

[1] Y. Liu, W. Liu, Y. Wu, and H. Yu, (2025) *"Distributed Voltage Optimal Control Method for Energy Storage Systems in Active Distribution Network"* **Energies *18***(14): 3670. DOI: 10.3390/en18143670.

[2] Z. Zhang, X. Guo, P. Yang, T. Wang, Y. Ji, and L. Yao, (2024) *"Line Loss Calculation and Optimization in Low Voltage Lines with Photovoltaic Systems Using an Analytical Model and Quantum Genetic Algorithm"* **Tehnički vjesnik *31***(2): 486–494. DOI: 10.17559/TV-20230516000638.

[3] F. Yuan, Y. Lu, Z. Xie, and S. Dai, (2024) *"Distributed Photovoltaic Distribution Voltage Prediction Based on eXtreme Gradient Boosting and Time Convolutional Networks"* **IEEE Access *12***: 177576–177588. DOI: 10.1109/ACCESS.2024.3502759.

[4] J. Yang, S. Zhu, and T. Zhou, (2024) *"Distributed Model Predictive Control for Voltage Coordination of Distributed Photovoltaic Distribution Networks with High Permeability"* **Journal of Applied Science and Engineering *28***(6): 1341–1350. DOI: 10.6180/jase.202506_28(6).0016.

[5] H. Pei, G. Yan, Y. Zhao, W. Zhang, and C. Xiao, (2025) *"Research on Harmonic Optimization and Suppression of Distributed Photovoltaic Storage and Distribution Networks by Improving PSO"* **Frontiers in Mechanical Engineering *11***: 1667908. DOI: 10.3389/fmech.2025.1667908.

[6] H. Shi et al., (2025) *"A Novel Hosting Capacity Evaluation Method for Distributed PV Connected in Power System Based on Maximum Likelihood Estimation of Harmonic"* **IEEE Journal of Photovoltaics *15***(3): 500–508. DOI: 10.1109/JPHOTOV.2025.3541402.

[7] S. Sun, S. Yang, P. Yu, Y. Cheng, J. Xing, Y. Wang, Y. Yi, Z. Hu, L. Yao, and X. Pang, (2025) *"A Reinforcement Learning-Based Approach for Distributed Photovoltaic Carrying Capacity Analysis in Distribution Grids"* **Energies *18***(18): 5029. DOI: 10.3390/en18185029.

[8] S. Rong et al., (2024) *"Adaptive Modeling and Analysis of Distributed Photovoltaic Absorptive Capacity Based on Improved Simulated Annealing Algorithm"* **International Journal of Low-Carbon Technologies *19***: 2032–2039. DOI: 10.1093/ijlct/ctae071/7745528.

[9] W. Hao, W. Xiao, Q. Yan, Q. Jia, B. Hu, and P. Li, (2024) *"Evaluation of Distributed Photovoltaic Economic Access Capacity in Distribution Networks Considering Proper Photovoltaic Power Curtailment"* **Energies *17***(17): 4441. DOI: 10.3390/en17174441.

[10] Y. Zheng, K. Zhou, Y. Yang, H. Diao, L. Hua, R. Wang, K. Liu, and Q. Guo, (2025) *"Robust Assessment Method for Hosting Capacity of Distribution Network in Mountainous Areas for Distributed Photovoltaics"* **Energies *18***(9): 2394. DOI: 10.3390/en18092394.

[11] S. Liu, Y. Xie, Z. Jiang, et al., (2025) *"Expansion Planning of Photovoltaic-Storage for Distribution Networks Based on Distributionally Robust Optimization"* **Chinese Journal of Electrical Engineering *11***(4): 163–175. DOI: 10.23919/CJEE.2025.000113.

[12] C. Gong, W. Wang, W. Zhang, N. Dong, X. Liu, Y. Dong, and D. Zhang, (2024) *"Active Power Optimisation Scheduling Method for Large-Scale Urban Distribution Networks with Distributed Photovoltaics Considering the Regulating Capacity of the Main Network"* **Frontiers in Energy Research *12***: 1450986. DOI: 10.3389/fenrg.2024.1450986.

[13] M. Kou et al., (2026) *"Optimized Dispatch of Distribution Networks Considering Distributed Photovoltaic Uncertainty and Distributed Pumped Storage"* **Recent Advances in Electrical and Electronic Engineering *19***(1): 1–16. DOI: 10.2174/0123520965377072250421074450.

[14] B.-X. Ji, H.-H. Liu, P. Cheng, X.-Y. Ren, H.-D. Pi, and L.-L. Li, (2024) *"Phased Optimization of Active Distribution Networks Incorporating Distributed Photovoltaic Storage System: A Multi-Objective Coati Optimization Algorithm"* **Journal of Energy Storage *91***: 112093. DOI: 10.1016/j.est.2024.112093.

[15] J. Li, X. Zhou, Y. Zhou, et al., (2024) *"Optimal Configuration of Distributed Generation Based on an Improved Beluga Whale Optimization"* **IEEE Access *12***: 31000–31013. DOI: 10.1109/ACCESS.2024.3368440.

[16] K. Zhang, Y. Cui, Y. Wei, W. Wang, Y. Yue, and Y. Zhang, (2025) *"Research on Distributed Photovoltaic Efficient Digestion Method Based on Optical Storage Direct Flexible Mode"* **Energy Reports *13***: 4926–4935. DOI: 10.1016/j.egyr.2025.04.018.

[17] G. Lei, B. He, J. Zhang, C. Liu, Z. Li, W. Dai, Y. Liu, and M. Wang, (2025) *"Location and Sizing of Distributed Energy Storage in Distribution Substations under Multiple Scenarios Based on Improved Affinity Propagation Clustering"* **Electric Power Systems Research *248***: 111898. DOI: 10.1016/j.epsr.2025.111898.

[18] X. Zhang, J. Wang, J. Wang, H. Wang, and L. Lu, (2024) *"Enhanced LSTM-Based Robotic Agent for Load Forecasting in Low-Voltage Distributed Photovoltaic Power Distribution Network"* **Frontiers in Neurorobotics *18***: 1431643. DOI: 10.3389/fnbot.2024.1431643.

[19] J. Zhang, B. Li, F. Chen, B. Li, X. Ji, and F. Xiao, (2024) *"Multi-Terminal Negative Sequence Directional Pilot Protection Method for Distributed Photovoltaic and Energy Storage Distribution Network"* **International Journal of Electrical Power & Energy Systems *157***: 109855. DOI: 10.1016/j.ijepes.2024.109855.

[20] M. Zhang, J. Liu, Y. Liu, L. Xia, C. Chai, and P. Li, (2024) *"Lightning Risk Assessment of Active Distribution Network with Distributed Photovoltaic System"* **Energy Reports *12***: 3711–3717. DOI: 10.1016/j.egyr.2024.09.045.

[21] M. Wang, R. Li, Y. Shi, X. Zhang, Y. Liu, and Q. Fang, (2026) *"Intelligent Prediction of Grid Connection Point Voltage Overrun for Distributed Photovoltaic Generation Systems"* **Electric Power Systems Research *252***: 112361. DOI: 10.1016/j.epsr.2025.112361.